minerals

MDPI

Article

In Situ Trace Element and S-Pb Isotope Study of Pyrite from the Denggezhuang Gold Deposit in the Jiaodong Peninsula—Insights into the Occurrence of Gold and the Source of Ore-Forming Materials

Junjin Zhang [1,2,3], Zhengjiang Ding [1,3,*], Junwei Bo [2,3], Pan Ji [2], Tingting Li [2] and Wei Xin [4]

[1] School of Resources and Environmental Engineering, Shandong University of Technology, Zibo 255000, China; zhjj109@163.com

[2] Shandong Provincial No. 3 Exploration Institute of Geology and Mineral Resources, Yantai 264004, China; bojunwei@126.com (J.B.); achievewish@163.com (P.J.); 13365351845@163.com (T.L.)

[3] Shandong Provincial Engineering Laboratory of Application and Development of Big Data for Deep Gold Exploration, Weihai 264209, China

[4] Research Center of Continental Dynamics, College of Earth Science and Engineering, Shandong University of Science and Technology, Qingdao 266590, China; skd996362@sdust.edu.cn

[*] Correspondence: dingzjdikuang@163.com

Abstract: The Jiaodong gold province is one of the most important gold fields globally and the largest in China. The Denggezhuang gold deposit is situated in the eastern portion of the Muping metallogenic belt, within the Jiaodong gold province. Despite many recent investigations, detailed mineralogical studies, particularly on auriferous minerals such as pyrite, are lacking. Therefore, further constraints on the occurrence mode and source of gold are necessary for this deposit. This study employed in situ laser ablation (multi-collector) inductively coupled plasma mass spectrometry (LA-MC-ICP-MS) trace element and sulfur-lead isotopic analyses on pyrite at different stages. The aim was to reveal the occurrence status of various trace elements within Denggezhuang pyrite and to trace the complete evolution process of multi-stage fluids at Denggezhuang, elucidating the sources of gold mineralization. Four generations of pyrite in chronological order, Py-1, Py-2a, Py-2b, and Py-3, were identified via petrographic and backscattered electron (BSE) image analyses. Using in situ LA-MC-ICP-MS, we found that Co and Ni are most abundant in Py-1, while Py-2b is rich in As, Au, Ag, Pb, and Zn, reflecting the evolution of the mineralizing fluids in different mineralization stages. Py-2b contains a significant amount of invisible lattice gold, which migrates and precipitates within fluids rich in As. The in situ LA-MC-ICP-MS S-Pb isotopic analysis of pyrite indicates a relatively consistent source of ore-forming materials across different stages. Additionally, the S-Pb isotope characteristics resemble those of widely distributed coeval mafic dikes. Therefore, we propose that a water-rich, fertile, and deep-seated mafic magmatic system might have provided fluids, materials, and heat for mineralization.

Keywords: Jiaodong gold province; Denggezhuang gold deposit; pyrites; ore-forming materials

1. Introduction

The Jiaodong Peninsula in the eastern part of the North China Craton (NCC) has proven gold reserves exceeding 5000 tons, making it one of the most significant gold provinces globally and the largest in China [1]. In recent years, extensive studies have been conducted on various gold deposits in the Jiaodong region, constraining the timing of gold mineralization events, the physicochemical conditions of mineralization, the properties of ore-forming fluids, gold deposition mechanisms, and the mineralization process, e.g., [1–6]. Gold deposits in Jiaodong typically exhibit multiple mineralization stages, possibly attributed to a single fluid, e.g., [7] or multi-stage fluids [8]. However, the sources of fluids in

different stages remain unclear. Furthermore, many orogenic gold deposits host high-grade gold ores [9,10], often associated with arsenopyrite and/or pyrite. Yet, there has been relatively limited research on the relationship between gold mineralization and arsenic in the Jiaodong region [11], with the existing research primarily focusing on visible gold and less attention being paid to invisible gold. Recently, arsenic-bearing pyrites with an arsenic content up to 1.4 wt.% and relatively high invisible gold content (up to 36 ppm) were discovered in the Denggezhuang deposit. Hence, this presents an opportunity to study the behavior of gold and arsenic during gold mineralization and gain a better understanding of the sources of gold mineralization mechanisms in this deposit. Additionally, it is worth noting the recent advancements in microanalytical techniques such as electron microprobe (EMP) analysis, laser ablation inductively coupled plasma mass spectrometry (LA-ICP-MS), secondary ion mass spectrometry (SIMS), and nanoscale SIMS. These techniques can reveal isotopic information within individual pyrite grains with complex internal microstructures [9,12–14]. Such information aids in constraining the growth history of pyrite and inferring the sources, properties, and evolution of related ore-forming fluids.

This study conducted detailed petrographic investigations on different generations of pyrite, along with in situ LA-MC-ICP-MS trace element and sulfur-lead isotope analyses. This study aims to elucidate the occurrence status of various trace elements in pyrites found within the Denggezhuang deposit and to identify their sources of multi-stage fluids within the Denggezhuang deposit.

2. Regional and Deposit Geology

The Jiaodong Peninsula is situated at the eastern edge of the North China Craton (NCC), delineated by the Tan-Lu Fault at the western edge (see Figure 1). The North China Craton is one of the oldest ($\geq$3.8 Ga) and largest cratons globally, spanning approximately 1.5 million square kilometers [15]. It has undergone various tectonic movements and reactivation/de-cratonization events since the Archean Eon, particularly during the Mesozoic Era, resulting in lithospheric thinning (~120 km) and widespread magmatism, deformation, and magmatic-hydrothermal events [16]. These thermotectonic events within the North China Craton have generated extensive gold mineralization [17,18], mainly concentrated in regions such as the Liaodong Peninsula, Jiaodong Peninsula, Inner Mongolia, and Hebei and Henan provinces.
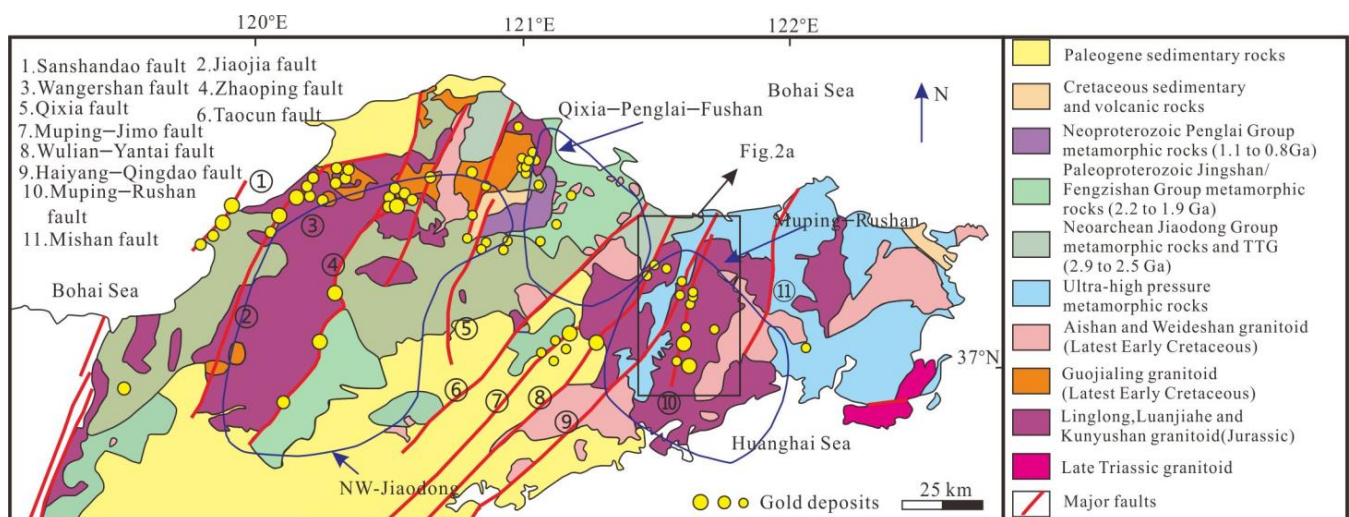

Figure 1. Sketch geologic map of the Jiaodong Peninsula, revised after Song et al., (2020) [19].

The Jiaodong Peninsula represents China's largest gold province (reserves > 5000 tons), accounting for over 40% of China's total gold reserves [19,20]. It is the world's third-largest gold mineralization region, following only the Witwatersrand Basin (South Africa) and the Muruntau region (Uzbekistan) [21]. The peninsula primarily comprises Precam-

brian crystalline basement rocks and Mesozoic volcanic rocks, with minor occurrences of Paleogene-Neogene volcanic rocks and Quaternary sediments [19] (refer to Figure 1). The Precambrian basement primarily consists of Neoproterozoic Jiaodong Group, Paleoprotero-zoic Jingshan Group, Fenzishan Group, and Mesoproterozoic Penglai Group sedimentary metamorphic rock units [21]. Mesozoic volcanic rocks are predominantly found in the Jiaolai Basin, which includes the Wangshi Group, Qingshan Group, and Laiyang Group [22]. The Mesozoic magmatism also includes widespread occurrences of granitic and medium-to coarse-grained syenitic veins, mainly established within the Jurassic and Cretaceous periods. Jurassic plutons (167–157 Ma) [23,24] mainly comprise calc-alkaline diorite, granite diorite, and biotite granite (e.g., Linglong, Luanjiahe, Kunyushan, and Wendeng plutons). Cretaceous intrusions (130–110 Ma) [25,26]; predominantly include granodiorite, granite diorite, and syenite (e.g., Guojialing and Weideshan plutons). The region features well-developed fault systems trending in a northeasterly to north–northeasterly direction, with many gold deposits located along these faults (see Figure 1). Previously, Jiaodong gold deposits were categorized into three metallogenic belts from west to east: Jiaodong North-west (Northwest), Qixia-Penglai-Fushan, and Muping-Rushan (as shown in Figure 1). The gold deposits in the Jiaodong Peninsula often manifest as disseminated networks and/or vein-like structures associated with the alteration of quartz-sericite-pyrite veins or quartz-carbonate veins [20]. Most gold deposits occur along regional faults or their secondary branches [27,28]. These deposits commonly exhibit sericitization, silicification, carbonation, potassic feldspar alteration, and sulfidation. Therefore, the mineral assemblage is quite similar, including quartz, sericite, carbonates, sulfides, hydrothermal feldspar, and minor amounts of sulfosalts. Gold typically occurs in the form of native gold associated with fractured sulfides or quartz. The formation age of Jiaodong gold deposits is estimated to be around 120 ± 5 million years ago, supported by various dating methods such as sericite Ar-Ar, pyrite Rb-Sr, and monazite U-Pb dating [20].

The Denggezhuang gold deposit is situated within the Su-Lu Ultrahigh Pressure Belt in the eastern part of the Jiaodong Peninsula, approximately 30 km south of Muping District in Yantai City. It holds gold reserves exceeding 50 tons and is the second-largest quartz vein-type gold deposit in the Muping-Rushan metallogenic belt of the Jiaodong Peninsula (see Figure 2a). The surrounding rock of the ore body's roof and bottom plate is mainly composed of mozongranite, along with a small amount of lamprophyre, and locally includes medium- to coarse-grained granodiorite (see Figures 2b and 3). The Jinniushan Fault is the main trunk fault in the region. Coeval secondary oblique-slip fault structures intersecting with Jinniushan, especially the north–northeastern-oriented fault structures intersecting with faults in other directions, represent favorable ore-forming sites for gold deposits. The Denggezhuang gold deposit comprises multiple mineralized zones, with the primary occurrences being within the number I and II mineralized zones, displaying branching, intersection, and lensoid phenomena (see Figure 2). The shapes of the ore bodies are mainly lens-like and vein-like outcroppings in the mineralized zones. The number I metallogenic belt is located on the eastern side of the mining area. The exposed length in the area is approximately 2000 m, with its width ranging from 1 m to 26 m. It has a trend of 10° to 25°, dipping to the northwest at an angle of 40° to 89° (Figure 3). Alteration within the zone is well developed, mainly characterized by silicification, sericitization, pyritization, potash feldspathization, and carbonate mineralization, with a small amount of chloritization. Lamprophyre dikes and the mineralized alteration zone are roughly parallel in occurrence. The main ore mineral within the ore body is pyrite, although minor amounts of chalcopyrite, galena, sphalerite, and gold-bearing minerals are also present, while the gangue minerals consist mainly of quartz, along with lesser amounts of plagioclase, sericite, and calcite. The alteration of the surrounding rocks is well developed, primarily featuring silicification, sericitization, pyritization, potassic feldspar alteration, carbonatization, and minor chloritization. The alteration zones exhibit distinct zonation characteristics: from the gold-bearing quartz vein (ore body) outward, the alteration

assemblage progresses in the following order: (pyrite) sericite alteration–potassic (hematite) alteration–unaltered granite.
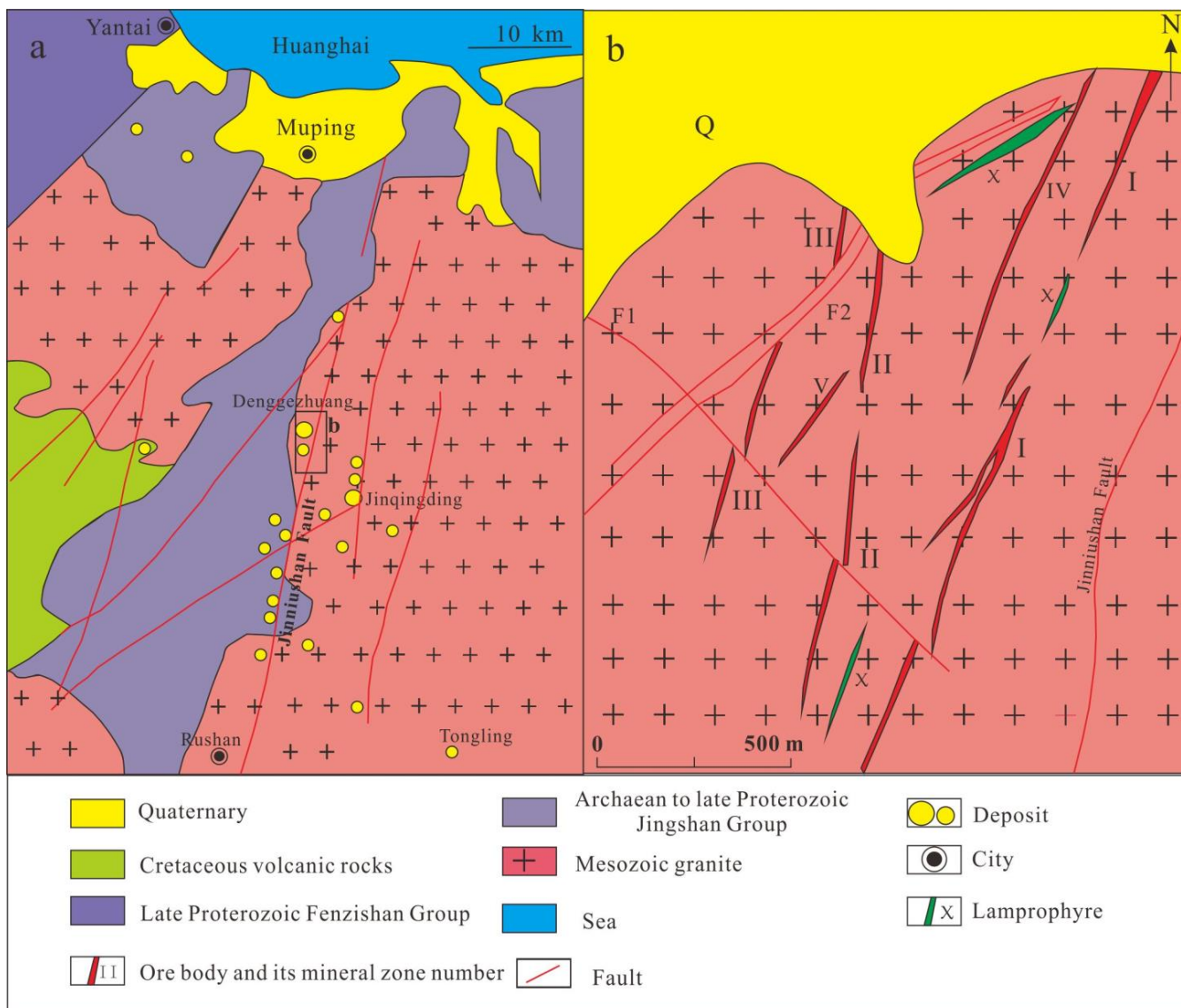

Figure 2. (**a**) Geological sketch map of the Muping-Rushan gold belt in the Jiaodong Peninsula, revised after Xue et al. (2018) [29]; (**b**) Geological map of the Denggezhuang gold deposit, revised after Xue et al. (2014) [30].

Based on field observations and microscopic analysis, in addition to potassic alteration stage, the hydrothermal mineralization period is divided into four main stages from early to late: V1–V4 (refer to Figure 4).

Potassic alteration stage: Intense hydrothermal alteration resulted in the extensive alteration of plagioclase to potassium feldspar. Potassic alteration envelopes plagioclase and quartz, with the widespread development of potassium feldspar concentrated at the outermost zones of the ore bodies. It appears reddish in color, with a medium- to fine-grained structure and blocky texture. The mineral assemblage comprises quartz, potassium feldspar, plagioclase, and minor amounts of biotite, hematite, and pyrite.

V1 Stage (the quartz-pyrite stage): This stage marks the beginning of mineralization filling, representing the early phase of ore-forming processes. Ore-bearing hydrothermal fluids infiltrate and fill fault structures, and the mineral assemblage consists of abundant

pyrite within quartz. The pyrite particles are coarse-grained, exhibiting euhedral to subhedral granular shapes, predominantly cubic morphologies, and well-formed crystals. The quartz appears as milky white granular aggregates, forming subhedral crystals with relatively large grain sizes.
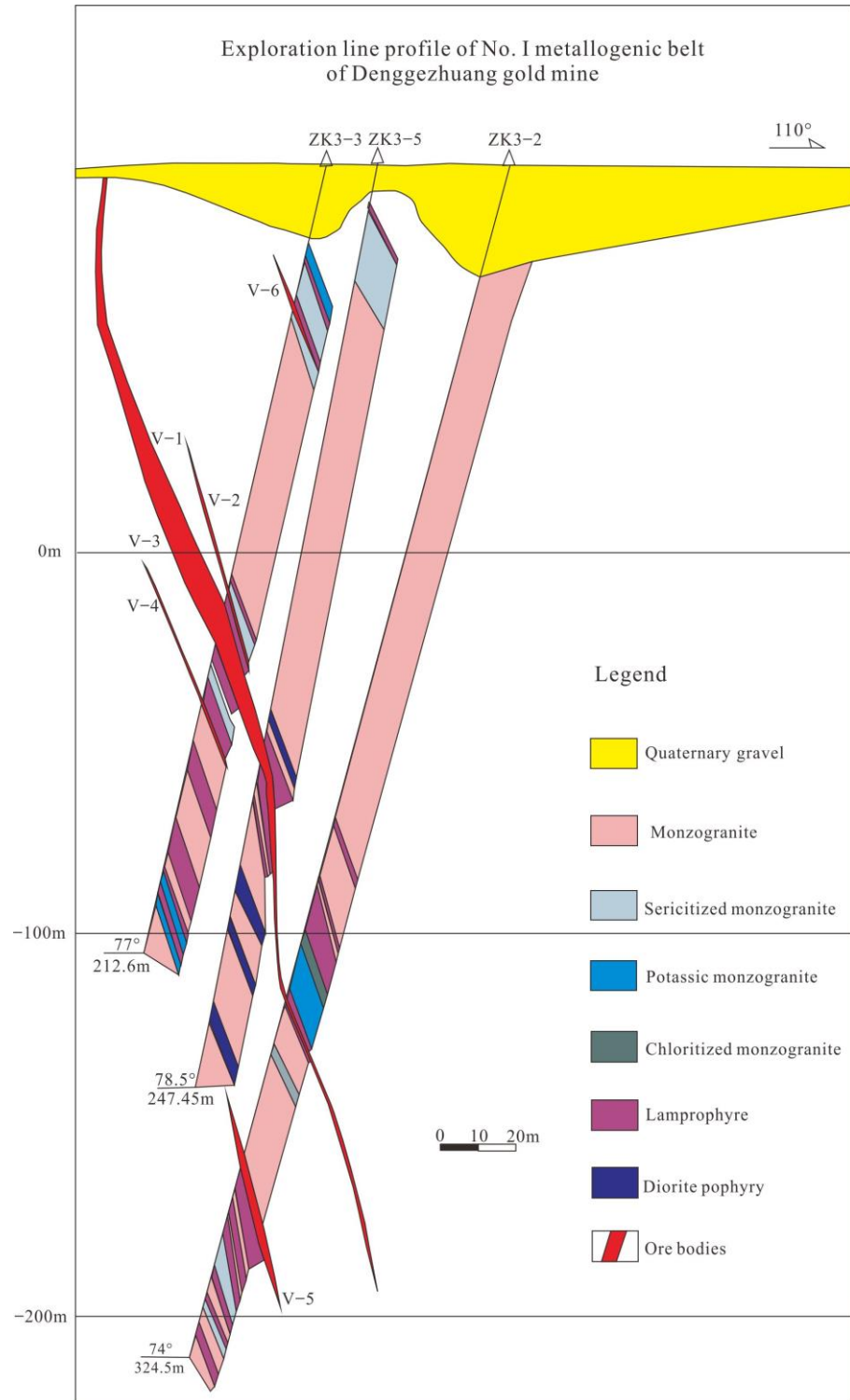

Figure 3. Geological cross-sections for the number I metallogenic belt in the Denggezhuang gold field (following Denggezhuang Gold Mine Detailed Investigation Report).

Stage (Vein) \ Mineral	Pre-ore		Syn-ore		Post-ore
	Potassic	V1	V2	V3	V4
Feldspar	████				
Quatz	████████	████	███		
Sericite		████	████		
Pyrite	── Py1	████	Py2 ███	Py3	Py4 ──
Gold		──	████		
Galena				── ████	
Chalcopyrite				── ████	
Pyrrhotite				── ████	
Sphalerite				████	
Dolomite				── ████	─
Calcite				──	████

Figure 4. Mineral paragenesis sequence of the Denggezhuang gold deposit.

V2 Stage (the quartz-auriferous pyrite stage): The mineral assemblage is dominated by pyrite and quartz. The pyrite grains are fine to medium (mostly 0.5–3 mm), irregularly shaped crystals that are mostly aggregates of irregular clusters, and some are subhedral. Surface alteration with limonite is commonly observed near the surface. Quartz is mostly smoky gray, with fine-grained, mostly euhedral to subhedral crystals. This stage exhibits a high gold content (up to 20 ppm), with native gold and silver-gold minerals being the main ores, marking the primary mineralization stage.

V3 Stage (the polymetallic sulfide stage): The mineral assemblage in this stage consists of pyrite, chalcopyrite, galena, sphalerite, magnetite, pyrrhotite, limonite, and quartz. Pyrite appears irregularly shaped and fine-grained, forming clusters or ribbon-like ore. Quartz is light ashy gray, exhibiting subhedral to euhedral shapes. Polymetallic sulfides are intimately associated with gold-silver minerals, occurring as cementation or as fine vein-like fillings within fractures of earlier stages.

V4 Stage (the quartz-carbonate stage): This stage is characterized by the abundant presence of carbonate minerals such as including siderite, ankerite, rhodochrosite, and quartz with low gold content. The sulfide content is low, and a small amount of pyrite is present.

Therefore, V1 represents the pre-mineralization stage, V2 and subsequent V3 represent the co-mineralization stage, and V4 represents the post-mineralization stage (Figure 4).

3. Samples and Analytical Techniques

A total of thirty-two polished sections were prepared from 18 samples collected from the Denggezhuang deposit. The samples were collected at the −120 m level from underground tunnels. These samples were used for optical microscopy and in situ analysis via laser ablation inductively coupled plasma mass spectrometry (LA–ICP–MS).

3.1. In Situ Sulfide Microanalysis for S Isotopes

The in situ sulfide sulfur isotopic testing was conducted at Wuhan SampleSolution Analytical Technology Co., Ltd., Wuhan, China, utilizing laser ablation multi-collector inductively coupled plasma mass spectrometry (LA-MC-ICP-MS). The laser ablation system employed was Geolas HD (Coherent, Dieburg, Germany) coupled with Neptune Plus (Thermo Fisher Scientific, Karlsruhe, Germany) for MC-ICP-MS. Helium gas served as the carrier gas in the laser ablation system. The analysis was performed in single-point mode to address the Down Hole fractionation effect during the sulfur isotope ratio analysis [31]. To mitigate this effect, a large spot size (44 μm) and low-frequency (2 Hz) laser conditions were selected, ablating approximately 100 laser pulses per analysis. A signal smoothing device was integrated to ensure stable signals at low frequency [32]. The laser energy density was fixed at 5.0 J/cm^2. Sulfur isotope mass fractionation was corrected using the SSB method. To prevent matrix effects, reference materials like PPP-1 were used for calibration with samples like pyrite, pyrrhotite, and pentlandite. Brass ore samples were calibrated using the national brass ore standard substance GBW07268 in powder form. Recommended $\delta^{34}S_{V\text{-}CDT}$ values for the above samples were referenced from Fu et al. (2016) [31]. For detailed instrument operational conditions and analytical testing methods, please refer to Fu et al. (2016) [31]. All analytical data underwent processing using the specialized isotope data processing software Icpmsdatacal 11.8 [33].

3.2. In Situ Sulfide Microanalysis for Pb Isotopes

The in situ analysis of sulfide Pb isotopes was carried out at Wuhan SampleSolution Analytical Technology Co., Ltd., Wuhan, China, using laser ablation multi-collector inductively coupled plasma mass spectrometry (LA-MC-ICP-MS). The laser ablation system used was Geolas HD (Coherent, Dieburg, Germany), while the MC-ICP-MS was Neptune Plus (Thermo Fisher Scientific, Karlsruhe, Germany). Helium gas was used as the carrier gas in the laser ablation system. The analysis was performed in single-point mode, and the spot size and ablation frequency of the laser were adjusted according to the sample's Pb signal intensity, typically ranging between 44 and 90 μm and 4 and 10 Hz. The laser energy density was maintained at approximately 5.0 J/cm^2. The analysis process was equipped with signal smoothing and a "mercury removal" device, which not only improved the signal stability and precision of isotopic ratio testing but also effectively reduced the gas background and sample's own Hg signals to ensure accurate determination of ^{204}Pb [32]. Sphalerite standard Sph-HYLM was used as an external standard to monitor the precision and accuracy of the analysis. The long-term accuracy for ^{208}Pb/^{204}Pb, ^{207}Pb/^{204}Pb, and ^{206}Pb/^{204}Pb was typically better than ±0.2 ‰, with external precision better than 0.4 ‰ (2σ). For detailed instrument operational conditions and analytical testing methods, refer to Zhang et al. (2016) [34]. All analytical data were processed using the specialized isotope data processing software Icpmsdatacal 11.8 [33].

3.3. In Situ Major and Trace Element Contents in Sulfides

The in situ analysis of major and trace element contents in sulfides was conducted at Wuhan SampleSolution Analytical Technology Co., Ltd., Wuhan, China, using LA-ICP-MS (Agilent Technologies, Inc., Santa Clara, CA, USA). Detailed instrument parameters and analytical procedures can be found in Zong et al. (2017) [35]. The GeolasPro laser ablation system comprised the COMPexPro 102 ArF 193 nm (Coherent, Santa Clara, CA, USA) excimer laser and MicroLas optics, coupled with an Agilent 7700e ICP-MS (Agilent Technologies, Inc., Santa Clara, CA, USA). During the laser ablation, helium was used as the carrier gas and argon was used as the compensation gas to adjust sensitivity. Both gases were mixed through a T-junction before entering the ICP, and the laser ablation system was equipped with a signal smoothing device [32]. The laser spot size and frequency for this analysis were set at 10 μm and 8 Hz, respectively. For single mineral trace element content treatment, calibration was performed using glass standard substances NIST 610 and NIST 612 (National Institute of Standards and Technology, Gaithersburg, MD, USA) for

multiple external standard corrections without internal standards [36]. The USGS sulfide standard substance, MASS-1, was used as a monitoring standard to verify the reliability of the calibration method. Offline processing of the analytical data, including selection of sample and blank signals, instrument sensitivity drift correction, and elemental content calculations, was conducted using the software ICPMSDataCal 11.8 (Wuhan, China) [36].

4. Results

4.1. Characteristics of Pyrite Mineralization

Four types of pyrite (Py-1 to Py-4) can be distinguished within the four stages (Figure 4). Type I pyrite (Py-1) crystals are distributed within the V1 stage vein (pre-ore) (Figure 5b). Py-1 crystals are predominantly medium- to coarse-grained (5–15 mm) with subhedral to euhedral crystal shapes (Figure 5d). These pyrite types exhibit microfractures. No association with gold is observed for Py-1, and its association with polymetallic sulfides is also minimal.
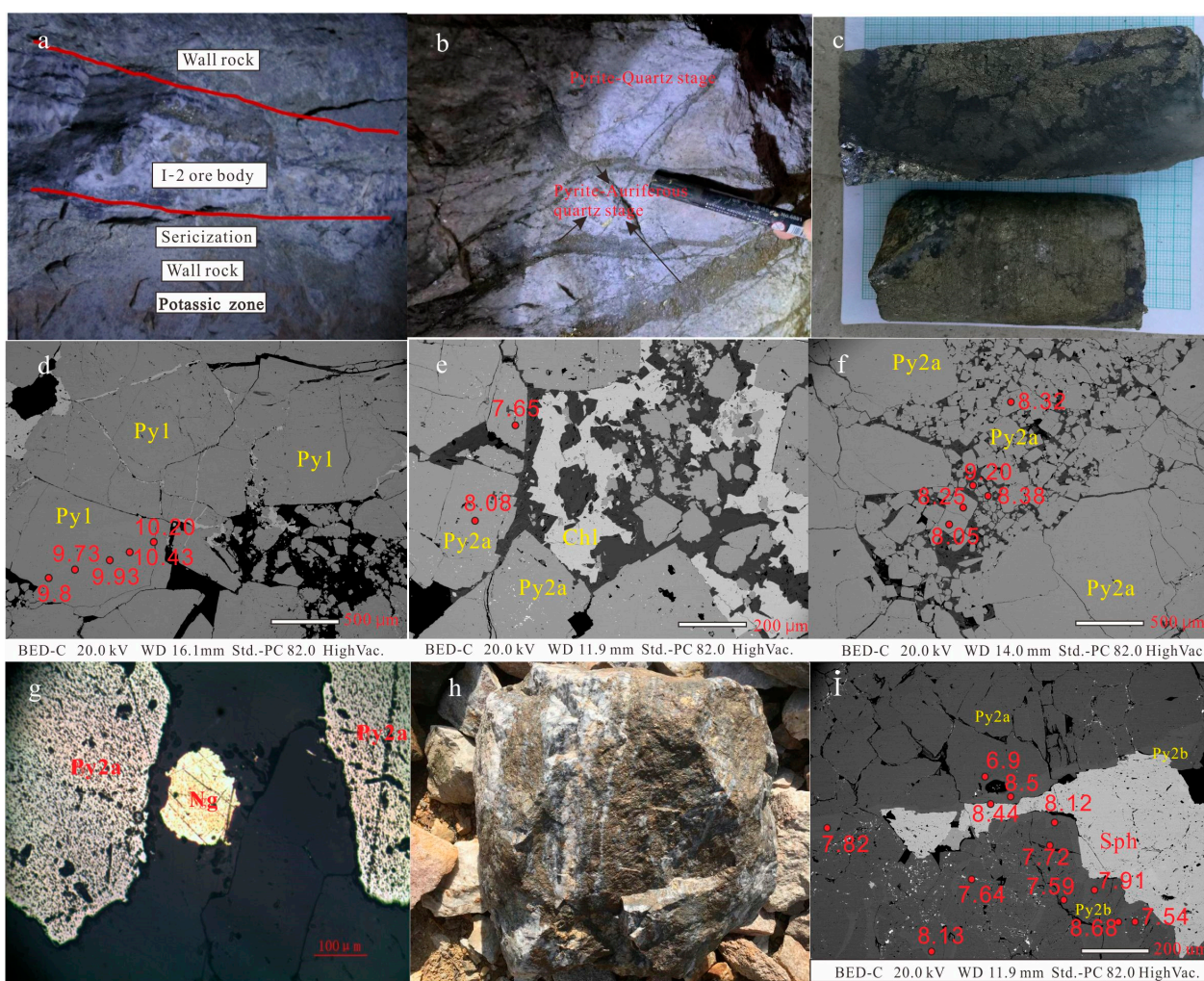

Figure 5. Microscope images of textures of metal minerals for different mineralization stages. (**a**) Underground photos of number I-2 ore body; (**b**) The cutting relationship between V1 (the quartz-pyrite stage) and V2 (the quartz-auriferous pyrite stage); (**c**) The cutting relationship between V3 (the polymetallic sulfide stage) and V2 (the quartz-auriferous pyrite stage); (**d**) Pyrite in V1 (Py-1) shows euhedral crystals with homogeneous brightness in the BSE, without mineral inclusions, porous microtextures, and oscillatory zones. (**e**,**f**) Pyrite of V2 and V3 (Py-2) is fine- to medium-grained and

euhedral-subhedral. Py2a shows little fracture, which is filled with gold and copper. (**g**) Natural gold in the stage of V2; (**h**) Hand specimen of polymetallic gold ore; (**i**) Py-2b sediments are deposited around Py-2a, with fewer pores and fissures and lack of mineral inclusions. The red dots and adjacent numbers represent the in situ sulfur isotopic analysis locations and results. Abbreviations: Py = pyrite, Sp = sphalerite, Ng = natural gold.

Pyrite-2 (Py-2) is one of the main sulfide minerals in the quartz-auriferous pyrite and polymetallic sulfide stage (Figure 5d–i). Py-2a crystals are mainly medium- to fine-grained (0.5–3 mm) and display subhedral to irregular crystal shapes (Figure 5e,f). This type of pyrite often grows with abundant mineral inclusions (such as galena, chalcopyrite, etc.) and/or sulfide-filled fractures, with few instances of corrosion features (Figure 5e–f). The distribution of native gold within the interstices of Py-2a indicates that this is the primary ore-forming stage for gold (Figure 5g). Some Py-2a crystals (portions with mineral inclusions) display rims, and these rims are labeled as Py-2b (Figure 5h) to distinguish them from Py-2a. Py-2b crystals surround Py-2a deposits, showing fewer pores, fractures, and a lack of mineral inclusions (Figure 5h). Py-2b crystals have considerably fewer pores and inclusions than those of Py-2a (Figure 5g).

Pyrite-3 (Py-3) occurs as fine-grained (0.5–3 mm) cubic crystals within late-stage veins (V4). This type of pyrite is primarily found in pyrite-rhodochrosite-quartz veins or fine veins. No association with gold or polymetallic sulfides is found for Py-3.

Based on the aforementioned crosscutting relationships, the four types of pyrite (Py-1, Py-2a, Py-2b, and Py-3) were assigned to four hydrothermal stages represented by three vein stages (V1 to V4) (Figure 3). Visible gold is only found in the V2 and V3 stages.

4.2. Geochemistry of Pyrite

The trace element compositions of Py-1 to Py-3 were obtained, comprising 5 points on Py-1, 26 points on Py-2, and 3 points on Py-3. All analyzed points targeted pyrite without visible mineral inclusions. The contents of Au, Ag, As, Co, Ni, Cu, Te, Pb, and Bi are listed in Table S1 and Figure 6.

The compositions of Py-1 show high Co and Ni concentrations, ranging from 23.6 to 496 ppm and 6.14 to 82.30 ppm, respectively, with Co/Ni values of 0.34–13.01. Au content varies between 0.0015 and 0.040 ppm, while the content of As ranges from 0.52 to 10.1 ppm. The Zn, Ag, and Pb concentrations are <1 ppm (median and mean values).

Composition of Py-2: Compared to Py-1, Py-2 exhibits significantly lower Ni and Co concentrations (<0.35 ppm and <0.13 ppm, respectively) (Table S1). The Au content of Py-2a ranges < 0.80 ppm, whereas the content of As varies between 655 and 17647 ppm. Their Cu, Pb, and Zn concentrations are a great deal higher than those of Py-1 (Figure 6c,d). Py-2b shows an Au content ranging from 0.23 to 36.2 ppm and As content ranging from 276 to 13,950 ppm.

Composition of Py-3: Compared to Py-1 and Py-2, Py-3 is low in Ni and Co contents (<0.034 ppm and <0.030 ppm, respectively) (Table S1). The Au content of Py-3 ranges from 0.015 to 0.030 ppm, while the content of As varies between 2.6 and 27.3 ppm. Their Cu, Pb, and Zn concentrations are comparable to those of Py-2a but lower than those of Py-2b (Figure 6c,d).

Upon pooling all pyrite samples together, Au shows a strong positive correlation with As in the Denggezhuang deposit, displaying extensive concentration ranges (Figure 6a), whereas no correlation is found between Au and As in the Linglong gold deposit. Moderate positive correlations are observed between Ag and Pb in Py-2 in both the Linglong and Denggezhuang deposits (Figure 6f). Furthermore, the correlation between gold and other elements is very weak (Figure 6b–e).
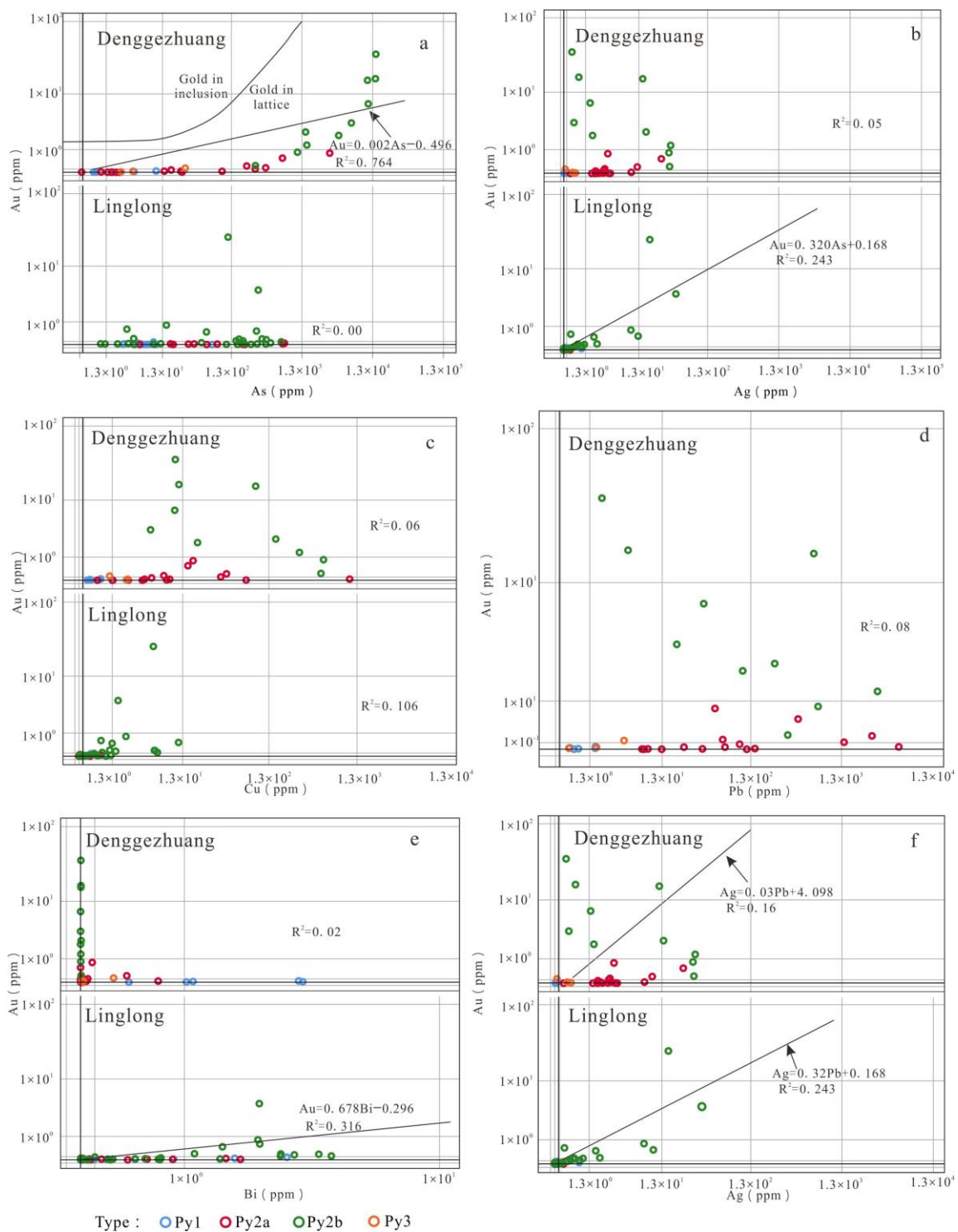
Figure 6. Elemental correlations for pyrites of different stages from the Denggezhuang gold deposit. (**a**) Plots of Au vs. As; (**b**) Plots of Au vs. Ag; (**c**) Plots of Au vs. Cu; (**d**) Plots of Au vs. Cu; (**e**) Plots of Au vs. Cu; (**f**) Plots of Au vs. Cu; R^2 represents linear correlation, and a lower numerical value indicates a weaker correlation. Pyrite data of Linglong gold deposit using As a reference [37]. Au saturation lines in pyrite are taken from Reich et al. (2005) [38].

4.3. In Situ S-Pb Isotopic Composition

The in situ $\delta^{34}S$ values of pyrite separated from the Denggezhuang deposit exhibit a narrow range, ranging from +6.9‰ to +10.4‰, as presented in Table S1 and depicted in Figure 7. The $\delta^{34}S$ values of Stage I pyrite range from +9.4‰ to +10.4‰, while the $\delta^{34}S$

values of Py-2a range from +6.9‰ to +9.2‰. Additionally, the δ^{34}S values of Py-2b range from +7.5‰ to +8.7‰, and the δ^{34}S values of Py-3 range from +7.5‰ to +8.7‰.
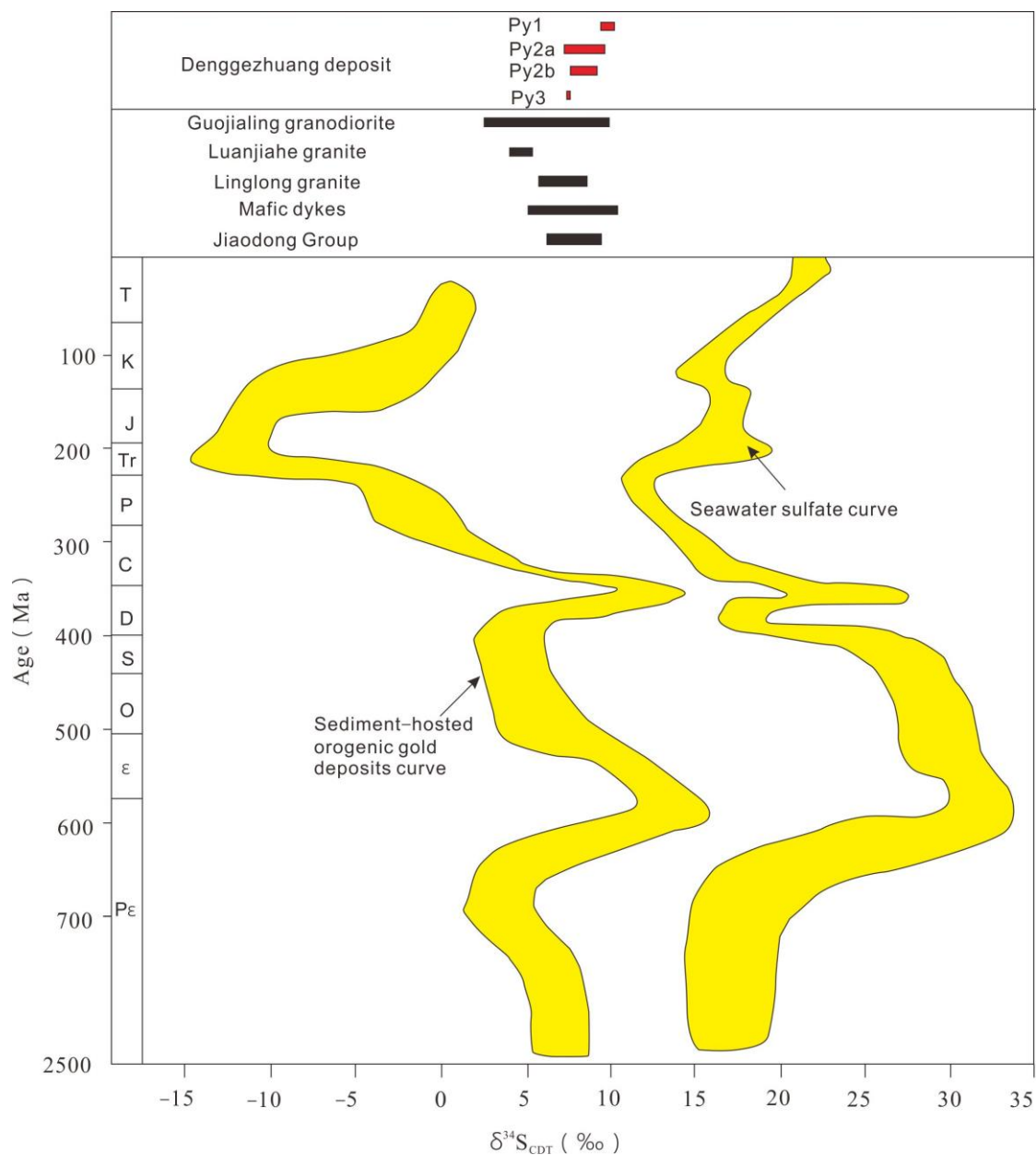

Figure 7. Diagrams of the sulfur isotopic composition of pyrites from the Denggezhuang gold deposit and regional rocks. The sulfur isotopic data are taken from Mao et al. (2008) [39], Wen et al. (2015) [40], Yang et al. (2016) [5], Cai et al. (2018) [28], and Deng et al. (2019) [41]. Sulfur isotopic compositions of sulfides in global sediment-hosted orogenic gold deposits through geologic time that relate to the time-dependent marine sulfate curve [42,43]. The ranges of major geologic units are taken from Yang et al. (2014) [44].

The Pb isotopic compositions of pyrite are listed in Table S1 and graphically depicted in Figure 8. The Pb isotopes from ten pyrite samples of Py-2a yield ^{206}Pb/^{204}Pb values ranging from 16.994 to 17.155, ^{207}Pb/^{204}Pb values ranging from 15.419 to 15.494, and ^{208}Pb/^{204}Pb values ranging from 37.444 to 37.640. Meanwhile, six pyrite samples from Py-2b yield ^{206}Pb/^{204}Pb values ranging from 16.971 to 17.045, ^{207}Pb/^{204}Pb values ranging from 15.402 to 15.447, and ^{208}Pb/^{204}Pb values ranging from 37.368 to 37.511. The Pb isotopic

ranges of the two types of pyrite are close, resembling similar types of gold deposits in the Jiaodong region.
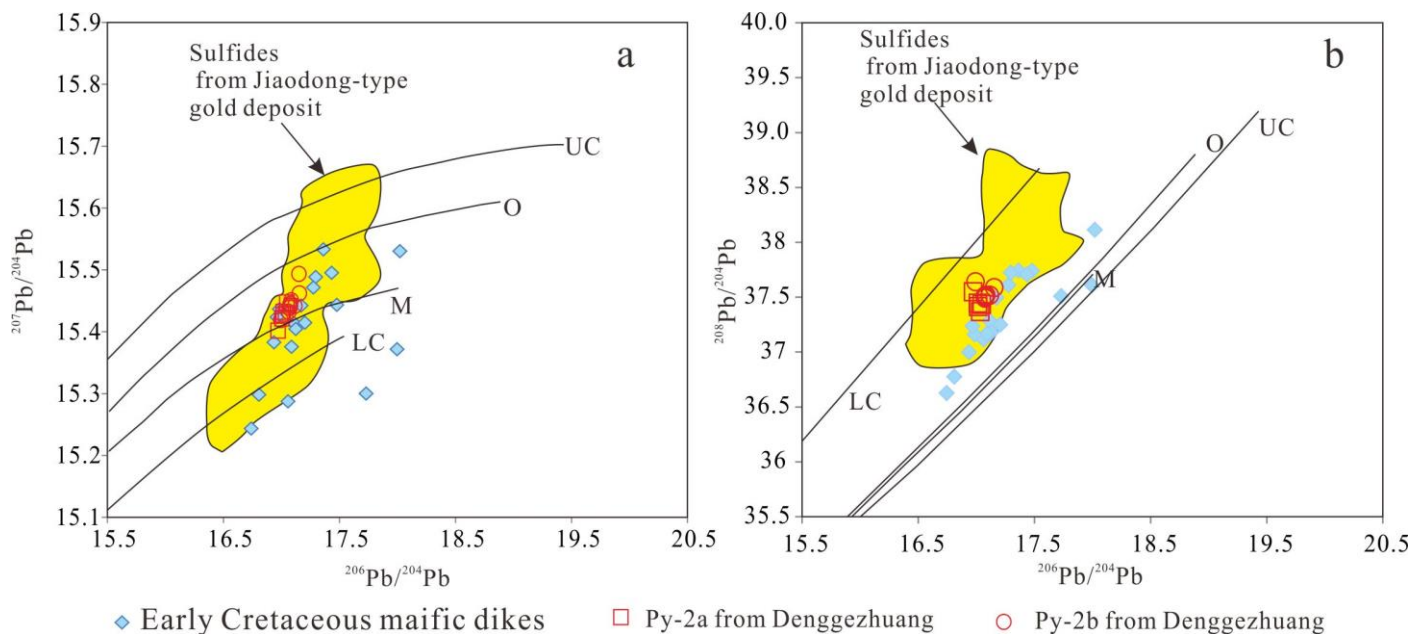

Figure 8. Plots of $^{206}Pb/^{204}Pb$ vs. $^{207}Pb/^{204}Pb$ (**a**); $^{206}Pb/^{204}Pb$ vs. $^{208}Pb/^{204}Pb$ (**b**) [45]. UC: upper crust, O: orogenic belt, M: mantle, LC: lower crust. The compiled dataset of the mafic dikes is according to Li et al. (2023) [18].

5. Discussion

5.1. Occurrence and Distribution of Gold

Within sulfides, trace elements can occur as solid solutions, nanoscale particles, and mineral inclusions [46–48]. Numerous studies emphasize the importance of distinguishing between solid solutions (within the lattice) and nanoscale particles [49,50]. Solid solutions or uniformly distributed minerals within mineral grains can generate smooth laser ablation spectra [49]. On the other hand, larger particles (>100 nm) can be identified as peaks in time-resolved laser ablation profiles. In this study, our point analyses and elemental maps of pyrite suggested no significant peaks in the concentrations of Au within pyrite (Figure 9), showing smooth laser ablation spectra that suggested the potential presence of Au within the mineral lattice.

Additionally, our LA-ICP-MS elemental maps and point analyses indicated variations in the concentrations of Co, Ni, and As within pyrite (Figure 6). Co and Ni were rich in Py-1, while the As content was higher in Py-2b (Figure 6). Notably, there was a significant difference in Au content between arsenian pyrite (Py-2b) and arsenic-free pyrite (Py-1), and Au showed a strong positive correlation with As (Figure 6a). Such positive correlations between As and Au have been acknowledged in several other deposits [9,38]. Reich et al. (2005) [38] identified a strong positive arsenic–gold correlation in pyrite from Carlin-type and epithermal deposits, concluding that the maximum gold content in the pyrite lattice depends on the arsenic content. They defined the empirical solubility of Au in arsenic-bearing pyrite as $C_{Au} = 0.02 \times C_{As} + 4 \times 10^{-5}$ [38], which can be represented by the Au saturation line on the Au vs. As diagram. All pyrite data in this study lay below the Au saturation line on the Au vs. As plot [38]. This indicated that Au was contained within the pyrite lattice (<250 nm) [51]. Pyrite grains with high As concentrations (>500 ppm As) are common in hydrothermal deposits, supporting a prevalent viewpoint that arsenic-rich sulfides play a role in sequestering Au^+ [38,52]. Therefore, the high As/Au values in Denggezhuang pyrite suggested that the As-rich ore fluids were largely undersaturated with respect to Au^0.
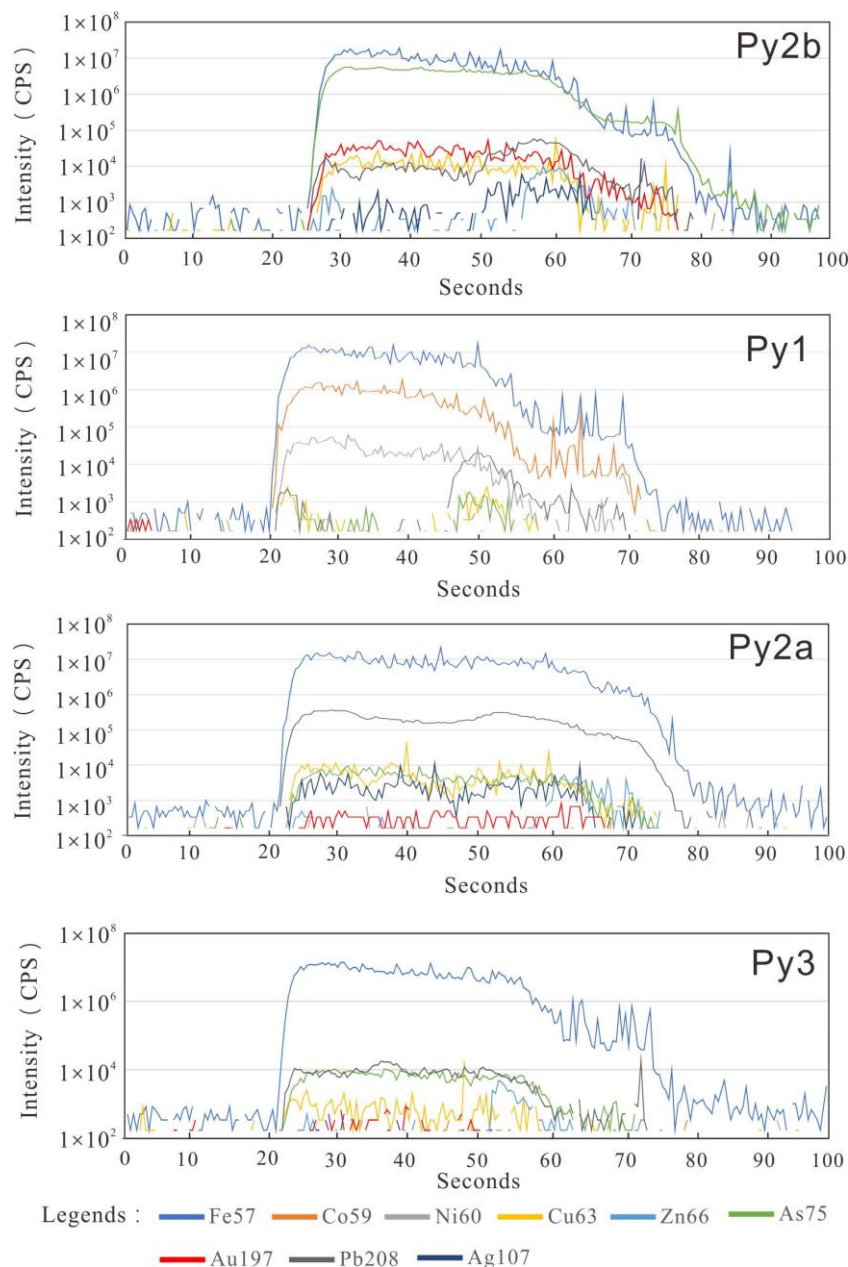
Figure 9. Representative time-resolved depth profiles, showing distributions of Fe, Co, Ni, Cu, Zn, As, Ag, Au, and Pb in various types of pyrites.

The gold in mesothermal deposits of the Jiaodong region is generally considered visible [53]. However, recent studies of some gold deposits in the Jiaodong gold province (Heilangou gold deposit, [11]; Zhuangzi gold deposit, [26]), as well as the current study, have revealed the importance of invisible gold. Hence, the occurrence and distribution of gold are significantly associated with the composition of ore fluids. Fluids rich in As [54,55] can sequester and transport more Au, whereas fluids with high Au/As values are often involved in invisible Au within the pyrite lattice.

5.2. Ore Material Sources

Previous studies have suggested that the $\delta^{34}S$ values of pyrite in Jiaodong-type gold deposits can represent the corresponding $\delta^{34}S$ values of ore-forming fluids, e.g., [11,28,39].

The results of our in situ sulfur isotopic analysis indicated that the $\delta^{34}S$ values of sulfides from the Denggezhuang deposit ranged from +6.9 to +10.4 ‰, with an average of

8.37 ‰ (*n* = 37). The sulfides mainly comprised pyrite, pyrrhotite, sphalerite, chalcopyrite, and galena. Considering the low temperature (177~361 °C) [29] and low f_{O2} of hydrothermal fluids (devoid of magnetite and hematite) [56], the sulfur isotopic characteristics of sulfides can represent a significant proportion of the sulfur isotopic composition of ore-forming fluids. The narrow and similar δ^{34}S values of Py-1 and Py-2 suggested that multiple pulses of hydrothermal fluids possibly originated from a common reservoir. Additionally, the narrow and similar δ^{34}S values of Py-1, Py-2, and Py-3 indicated that ore fluids from different mineralization stages likely shared a common sulfur source.

The δ^{34}S values of pyrite from the Denggezhuang gold deposit (6.07‰~8.33‰) overlapped with those of Late Jurassic biotite granodiorite (7.9‰~8.6‰) [39], Early Cretaceous granodiorite (2.7‰~10‰) [57], Early Cretaceous mafic intrusions (5.3‰~10.8‰) [57], and Late Archean metamorphic rocks of the Jiaodong Group (6.9‰~9.4‰; Figure 6) [58]. Hence, these geological bodies may have contributed to the mineralization of the Denggezhuang gold deposit.

However, the metamorphic age of the Jiaodong Group (1.9–2.2 Ga) [59] suggested that the devolatilization of metamorphic rocks occurred approximately 2 billion years ago, much earlier than the formation of Late Jurassic biotite granite (160–145 Ma) [24] and Early Cretaceous granodiorite (130~126 Ma) [23], which was earlier than the mineralization age (~120 Ma) [20]. The magmatic activities of Linglong and Guojialing granites preceded gold mineralization by at least approximately 10 million years, while the Aishan granite intrusion postdated the mineralization. At the scale of the mining area, the high-precision zircon U-Pb age of the Kunyu granite in the surrounding rock was found to be 155.8 million years [60], meaning that the rock predated the mineralization era.

Moreover, high δ^{34}S values might also result from seawater mixing [61] or progressive magma oxidation [62]. The absence of marine deposits from the Paleozoic to the Middle Mesozoic and lack of geological evidence to explain the Cretaceous sea level in the Jiaodong Peninsula [62] made the seawater mixing explanation unreasonable. However, Early Cretaceous mafic intrusions have close spatial and temporal relationships with gold mineralization in the Jiaodong gold district. The Denggezhuang gold deposit has an ore-forming age of 123 Ma [60]. The formation age of mafic intrusions related to the Linglong gold deposit is between 118 and 122 Ma [63]. Both the mafic intrusions and the Denggezhuang gold deposit exhibited similar sulfur isotopes, indicating that the ore-forming fluids from Early Cretaceous mafic intrusions originated from an enriched lithospheric mantle [64,65]. Deng et al. (2020) [20] suggested that the high δ^{34}S values of auriferous pyrite in the Sanshandao gold deposit of the Jiaodong Peninsula might have originated from the devolatilization of the lithospheric mantle, triggered by the early subduction events of the Yangtze Craton.

The slight differences in the Pb isotopic composition of pyrite suggested similar lead sources for various mineralization stages. From Figure 7, it can be observed that the Pb isotope data overlapped with the exposure range of mafic dikes, consistent with the Pb isotopic compositions of other gold deposits in the Jiaodong Peninsula. Given that the Pb-S isotopic characteristics of pyrite in the Denggezhuang gold deposit were similar to those of the widely distributed mafic dikes in the region, there is reason to believe that mafic rocks provided the material and fluid sources for mineralization.

In addition to S-Pb isotopic similarities, this pattern was also supported by the following facts. Firstly, the elements related to mineralization exhibited similar distribution patterns in the mafic dikes and ores. The metal ratios in sulfides within veins were similar to those in gold ores [66], and a significant correlation between the metal abundance ratios (Ag, As, Au, Bi, Co, Cu, Mo, Ni, Pb, Sb, and Zn) in diabase veins (120 Ma) and gold ores has been demonstrated in the Guocheng gold deposit of the Jiaodong gold district. Secondly, these mafic dikes are extensively distributed and closely associated with the temporal and spatial relationships of the ore bodies, typically manifesting in this mining area as mutual intercalation or sharing the same structural space (see Figure 2b). This close temporal and spatial relationship likely reveals their shared genetic association. Thirdly, the magmatic physicochemical conditions of the mafic dikes favored the formation of hydrothermal

deposits. Li et al. (2016) [67] suggested that the primitive magmas of Paleozoic-Cretaceous mafic dikes in the Jiaodong Peninsula were aqueous, volatile-rich, and ore component-rich, evolving under high-oxygen fugacity conditions. Fourthly, the mafic dikes contain abundant mineralization materials, supporting the formation of large-scale hydrothermal gold deposits. The analyzed gold content in the diabase veins associated with the same mineralization ranged from 0.04 to 3.59 ng/g, mainly remaining at 13 ng/g (*n* = 31) [68]. Lastly, the oxygen–hydrogen (OH) isotopic composition in Jiaodong gold ores is primarily distributed in the region between magmatic water and atmospheric precipitation [20], easily explained as a mixture of magmatic water and atmospheric water. The magmatic water was probably derived from the deep-seated parent magma of mafic dikes. Although the scale of the mafic dikes was small and insufficient to provide abundant ore-forming material, their widespread distribution suggested the existence of a large-scale mantle-derived magmatic supply system at depth, possibly extending deep towards the crust-mantle boundary. The cooling of this mafic magmatic system was adequate to provide sufficient gold and mineralizing fluids. Thus, mantle-derived mafic magma might have provided auriferous fluids for the Denggezhuang gold deposit, as well as other Jiaodong-type gold deposits. While we suggest that the mantle-derived magmatic activity represented by mafic veins provided ore-forming materials and fluids, this notion still needs to be validated in subsequent studies.

6. Conclusions

The conclusions we have drawn from our study are as follows:

(1) This study identified four types of pyrite (Py-1, Py-2a, Py-2b, and Py-3). Co and Ni are mainly distributed in Py-1, while Py-2b is significantly enriched in arsenic, silver (Ag), lead (Pb), and zinc (Zn), and has a gold (Au) content ranging from 6.71 to 36 ppm. Variations in elemental content reflect the distinct properties of ore-forming fluids across different mineralization stages.

(2) Pyrite within the Denggezhuang gold deposit contains a substantial amount of invisible lattice-bound gold, which was transported and precipitated within arsenic-rich fluids.

(3) Our in situ S-Pb isotopic analysis of pyrite indicates that a relatively consistent source of ore-forming materials was present across different stages. The aqueous and enriched deep-seated mafic-ultramafic magma chamber provided fluids, substances, and heat for mineralization.

References

1. Goldfarb, R.J.; Santosh, M. The dilemma of the Jiaodong gold deposits: Are they unique? *Geosci. Front.* **2014**, *5*, 139–153. [CrossRef]
2. Yang, J.H.; Zhou, X.H. Rb-Sr, Sm-Nd, and Pb isotope systematics of pyrite: Implications for the age and genesis of lode gold deposits. *Geology* **2001**, *29*, 711–714. [CrossRef]
3. Qiu, Y.; Groves, D.I.; McNaughton, N.J.; Wang, L.G.; Zhou, T. Nature, age, and tectonic setting of granitoid-hosted, orogenic gold deposits of the Jiaodong Peninsula, eastern North China craton, China. *Miner. Depos.* **2002**, *37*, 283–305. [CrossRef]
4. Fan, H.R.; Hu, F.F.; Yang, J.H.; Zhai, M.G. Fluid evolution and large-scale gold metallogeny during Mesozoic tectonic transition in the Jiaodong Peninsula, eastern China. *Geol. Soc. Lond. Spec. Publ.* **2007**, *280*, 303–316. [CrossRef]
5. Yang, L.Q.; Deng, J.; Wang, Z.L.; Guo, L.N.; Li, R.H.; Groves, D.I.; Zhao, H. Relationships between gold and pyrite at the Xincheng gold deposit, Jiaodong Peninsula, China: Implications for gold source and deposition in a brittle epizonal environment. *Econ. Geol.* **2016**, *111*, 105–126. [CrossRef]
6. Ma, W.D.; Fan, H.R.; Liu, X.; Pirajno, F.; Hu, F.F.; Yang, K.F.; Jiang, P. Geochronological framework of the Xiadian gold deposit in the Jiaodong province, China: Implications for the timing of gold mineralization. *Ore Geol. Rev.* **2017**, *86*, 196–211. [CrossRef]
7. Hu, H.; Liu, S.; Fan, H.R.; Yang, K.; Zuo, Y.; Cai, Y. Structural networks constraints on alteration and mineralization processes in the Jiaojia gold deposit, Jiaodong Peninsula, China. *J. Earth Sci.* **2020**, *31*, 500–513. [CrossRef]
8. Sun, W.; Feng, Y.; Lai, C.; Zhu, Z. A high-efficiency gold precipitation model associated with Fe carbonates: Example from the Jiudian deposit of the world-class Jiaodong gold province. *Ore Geol. Rev.* **2022**, *145*, 104894. [CrossRef]
9. Large, R.R.; Danyushevsky, L.; Hollit, C.; Maslennikov, V.; Meffre, S.; Gilbert, S.; Foster, J. Gold and trace element zonation in pyrite using a laser imaging technique: Implications for the timing of gold in orogenic and Carlin-style sediment-hosted deposits. *Econ. Geol.* **2009**, *104*, 635–668. [CrossRef]
10. Deditius, A.P.; Reich, M.; Kesler, S.E.; Utsunomiya, S.; Chryssoulis, S.L.; Walshe, J.; Ewing, R.C. The coupled geochemistry of Au and As in pyrite from hydrothermal ore deposits. *Geochim. Et Cosmochim. Acta* **2014**, *140*, 644–670. [CrossRef]
11. Feng, K.; Fan, H.R.; Hu, F.F.; Yang, K.F.; Liu, X.; Shangguan, Y.N.; Jiang, P. Involvement of anomalously As-Au-rich fluids in the mineralization of the Heilan'gou gold deposit, Jiaodong, China: Evidence from trace element mapping and in-situ sulfur isotope composition. *J. Asian Earth Sci.* **2018**, *160*, 304–321. [CrossRef]
12. Huston, D.L.; Sie, S.H.; Suter, G.F.; Cooke, D.R.; Both, R.A. Trace elements in sulfide minerals from eastern Australian volcanic-hosted massive sulfide deposits; Part I, Proton microprobe analyses of pyrite, chalcopyrite, and sphalerite, and Part II, Selenium levels in pyrite; comparison with delta 34 S values and implications for the source of sulfur in volcanogenic hydrothermal systems. *Econ. Geol.* **1995**, *90*, 1167–1196.
13. Ulrich, T.; Long DG, F.; Kamber, B.S.; Whitehouse, M.J. In situ trace element and sulfur isotope analysis of pyrite in a Paleoproterozoic gold placer deposit, Pardo and Clement Townships, Ontario, Canada. *Econ. Geol.* **2011**, *106*, 667–686. [CrossRef]
14. Tanner, D.; Henley, R.W.; Mavrogenes, J.A.; Holden, P. Sulfur isotope and trace element systematics of zoned pyrite crystals from the El Indio Au–Cu–Ag deposit, Chile. *Contrib. Mineral. Petrol.* **2016**, *171*, 1–17. [CrossRef]
15. Zhao, G.; Sun, M.; Wilde, S.A.; Li, S.Z. Late Archean to Paleoproterozoic evolution of the North China Craton: Key issues revisited. *Precambrian Res.* **2005**, *136*, 177–202. [CrossRef]
16. Zhu, R.X.; Fan, H.R.; Li, J.W. Decratonic gold deposits. *Sci. China Earth Sci.* **2015**, *58*, 1523–1537. [CrossRef]
17. Groves, D.I.; Goldfarb, R.J.; Santosh, M. The conjunction of factors that lead to formation of giant gold provinces and deposits in non-arc settings. *Geosci. Front.* **2016**, *7*, 303–314. [CrossRef]
18. Li, J.; Yang, Z.M.; Song, M.C.; Dong, L.L.; Li, S.Y.; Wang, R.S.; Liu, X.; Li, Z.S.; Song, Y.X.; Lai, C.K. Gold remobilization of the Sanshandao gold deposit, Jiaodong Peninsula, Eastern China: Perspective from in-situ sulfide trace elements and sulfur isotopes. *Ore Geol. Rev.* **2023**, 105505. [CrossRef]
19. Song, M.C.; Lin, S.Y.; Yang, L.Q.; Song, Y.X.; Ding, Z.J.; Li, J.; Zhou, M.L. Metallogenic model of Jiaodong Peninsula gold deposits. *Miner. Depos.* **2020**, *39*, 215–236.
20. Deng, J.; Yang, L.Q.; Groves, D.I.; Zhang, L.; Qiu, K.F.; Wang, Q.F. An integrated mineral system model for the gold deposits of the giant Jiaodong province, eastern China. *Earth-Sci. Rev.* **2020**, *208*, 103274. [CrossRef]
21. Song, M.; Ding, Z.; Zhang, J.; Song, Y.X.; Bo, J.W.; Wang, Y.Q.; He, C.Y. Geology and mineralization of the Sanshandao supergiant gold deposit (1200 t) in the Jiaodong Peninsula, China: A review. *China Geol.* **2021**, *4*, 686–719. [CrossRef]
22. Song, M.C.; Song, Y.X.; Ding, Z.J.; Li, S.Y. Jiaodong gold deposits: Essential characteristics and major controversy. *Gold Sci. Technol.* **2018**, *26*, 406–422, (In Chinese with English Abstract).
23. Yang, K.F.; Fan, H.R.; Santosh, M.; Hu, F.F.; Wilde, S.A.; Lan, T.G.; Liu, Y.S. Reactivation of the Archean lower crust: Implications for zircon geochronology, elemental and Sr–Nd–Hf isotopic geochemistry of late Mesozoic granitoids from northwestern Jiaodong Terrane, the North China Craton. *Lithos* **2012**, *146*, 112–127. [CrossRef]
24. Ma, L.; Jiang, S.Y.; Dai, B.Z.; Jiang, Y.H.; Hou, M.L.; Pu, W.; Xu, B. Multiple sources for the origin of Late Jurassic Linglong adakitic granite in the Shandong Peninsula, eastern China: Zircon U–Pb geochronological, geochemical and Sr–Nd–Hf isotopic evidence. *Lithos* **2013**, *162*, 251–263. [CrossRef]
25. Hou, M.L.; Jiang, Y.H.; Jiang, S.Y.; Ling, H.F.; Zhao, K.D. Contrasting origins of late Mesozoic adakitic granitoids from the northwestern Jiaodong Peninsula, east China: Implications for crustal thickening to delamination. *Geol. Mag.* **2007**, *144*, 619–631. [CrossRef]

26. Li, X.H.; Fan, H.R.; Zhang, Y.W.; Hu, F.F.; Yang, K.F.; Liu, X.; Zhao, K.D. Rapid exhumation of the northern Jiaobei Terrane, North China Craton in the Early Cretaceous: Insights from Al-in-hornblende barometry and U-Pb geochronology. *J. Asian Earth Sci.* **2018**, *160*, 365–379. [CrossRef]

27. Li, X.C.; Fan, H.R.; Santosh, M.; Hu, F.F.; Yang, K.F.; Lan, T.G. Hydrothermal alteration associated with Mesozoic granite-hosted gold mineralization at the Sanshandao deposit, Jiaodong Gold Province, China. *Ore Geol. Rev.* **2013**, *53*, 403–421. [CrossRef]

28. Cai, Y.C.; Fan, H.R.; Santosh, M.; Hu, F.F.; Yang, K.F.; Li, X.H. Decratonic gold mineralization: Evidence from the Shangzhuang gold deposit, eastern North China Craton. *Gondwana Res.* **2018**, *54*, 1–22. [CrossRef]

29. Xue, J.L.; Li, S.R.; Pang, Z.S.; Chen, H.; Sun, W.Y.; Tao, W.; Yao, L.; Zhang, Y.Q. Ore-forming fluids, sources of materials in the Denggezhuang gold deposit, Jiaodong Peninsula and implications for ore genesis. *Acta Petrol. Sin.* **2018**, *34*, 1453–1468.

30. Xue, J.L.; Li, S.R.; Sun, W.Y.; Zhang, Y.Q.; Zhang, X. Characteristics of the genetic mineralogy of pyrite and its significance for prospecting in the Denggezhuang gold deposit, Jiaodong Peninsula, China. *Sci. China* **2014**, *57*, 644–661. [CrossRef]

31. Fu, J.; Hu, Z.C.; Zhang, W.; Yang, L.; Liu, Y.; Li, M.; Hu, S. In situ, sulfur isotopes ($\delta34S$ and $\delta33S$) analyses in sulfides and elemental sulfur using high sensitivity cones combined with the addition of nitrogen by Laser Ablation MC-ICP-MS. *Anal. Chim. Acta* **2016**, *911*, 14–26. [CrossRef] [PubMed]

32. Hu, Z.C.; Zhang, W.; Liu, Y.S.; Gao, S.; Li, M.; Zong, K.Q.; Chen, H.H.; Hu, S.H. "Wave" Signal-Smoothing and Mercury-Removing Device for Laser Ablation Quadrupole and Multiple Collector ICPMS Analysis: Application to Lead Isotope Analysis. *Anal. Chem.* **2015**, *87*, 1152–1157. [CrossRef] [PubMed]

33. Zhang, W.; Hu, Z.C.; Liu, Y.S. Iso-Compass: New freeware software for isotopic data reduction of LA-MC-ICP-MS. *J. Anal. At. Spectrom.* **2020**, *35*, 1087–1096. [CrossRef]

34. Zhang, W.; Hu, Z.C.; Gunther, D.; Liu, Y.S.; Ling, W.L.; Zong, K.Q.; Chen, H.H.; Gao, S.; Xu, L. Direct lead isotope analysis in Hg-rich sulfides by LA-MC-ICP-MS with a gas exchange device and matrix-matched calibration. *Anal. Chim. Acta* **2016**, *948*, 9–18. [CrossRef] [PubMed]

35. Zong, K.Q.; Klemd, R.; Yuan, Y.; He, Z.; Guo, J.; Shi, X.; Zhang, Z. The assembly of Rodinia: The correlation of early Neoproterozoic (ca. 900 Ma) high-grade metamorphism and continental arc formation in the southern Beishan Orogen, southern Central Asian Orogenic Belt (CAOB). *Precambrian Res.* **2017**, *290*, 32–48. [CrossRef]

36. Liu, Y.S.; Hu, Z.C.; Gao, S.; Günther, D.; Xu, J.; Gao, C.; Chen, H. In situ analysis of major and trace elements of anhydrous minerals by LA-ICP-MS without applying an internal standard. *Chem. Geol.* **2008**, *257*, 34–43. [CrossRef]

37. Liang, Y.; Shu, L.; Ma, P.; Zhang, C.; Ma, Y.; Khan, M.; Shen, C. Gold source and ore-forming process of the Linglong gold deposit, Jiaodong gold province, China: Evidence from textures, mineral chemical compositions and sulfur isotopes of pyrite. *Ore Geol. Rev.* **2023**, 105523. [CrossRef]

38. Reich, M.; Kesler, S.E.; Utsunomiya, S.; Palenik, C.S.; Chryssoulis, S.L.; Ewing, R.C. Solubility of gold in arsenian pyrite. *Geochim. Et Cosmochim. Acta* **2005**, *69*, 2781–2796. [CrossRef]

39. Mao, J.; Wang, Y.; Li, H.; Pirajno, F.; Zhang, C.; Wang, R. The relationship of mantle-derived fluids to gold metallogenesis in the Jiaodong Peninsula: Evidence from D–O–C–S isotope systematics. *Ore Geol. Rev.* **2008**, *33*, 361–381. [CrossRef]

40. Wen, B.J.; Fan, H.R.; Santosh, M.; Hu, F.F.; Pirajno, F.; Yang, K.F. Genesis of two different types of gold mineralization in the Linglong gold field, China: Constrains from geology, fluid inclusions and stable isotope. *Ore Geol. Rev.* **2015**, *65*, 643–658. [CrossRef]

41. Deng, J.; Liu, X.; Wang, Q.; Dilek, Y.; Liang, Y. Isotopic characterization and petrogenetic modeling of Early Cretaceous mafic diking—Lithospheric extension in the North China craton, eastern Asia. *GSA Bull.* **2017**, *129*, 1379–1407. [CrossRef]

42. Goldfarb, R.J.; Miller, L.D.; Leach, D.L.; Snee, L.W. Gold Deposits in Metamorphic Rocks of Alaska. In *Mineral Deposits of Alaska*; Goldfarb, R.J., Miller, L.D., Eds.; Economic Geology Monograph: Littleton, CO, USA, 1997; pp. 151–190.

43. Chang, Z.; Large, R.R.; Maslennikov, V. Sulfur isotopes in sediment-hosted orogenic gold deposits: Evidence for an early timing and a seawater sulfur source. *Geology* **2008**, *36*, 971–974. [CrossRef]

44. Yang, L.Q.; Deng, J.; Wang, Z.L.; Chen, Y.T.; Jin, Z.M.; Shi, Y.L.; Zhu, R.X. Ore-controlling structural pattern of Jiaodong gold deposits: Geological-geophysical integration constraints. In *The Deep-Seated Structures of Earth in China*; Sciences Press Beijing: Beijing, China, 2014; pp. 1006–1030.

45. Zartman, R.E.; Doe, B.R. Plumbotectonics—The model. *Tectonophysics* **1981**, *75*, 135–162. [CrossRef]

46. Agangi, A.; Hofmann, A.; Wohlgemuth-Ueberwasser, C.C. Pyrite zoning as a record of mineralization in the Ventersdorp Contact Reef, Witwatersrand Basin, South Africa. *Econ. Geol.* **2013**, *108*, 1243–1272. [CrossRef]

47. Cook, N.J.; Ciobanu, C.L.; Mao, J. Textural control on gold distribution in As-free pyrite from the Dong**, Huangtuliang and Hougou gold deposits, North China Craton (Hebei Province, China). *Chem. Geol.* **2009**, *264*, 101–121. [CrossRef]

48. Fougerouse, D.; Micklethwaite, S.; Tomkins, A.G.; Mei, Y.; Kilburn, M.; Guagliardo, P.; Howard, D.L. Gold remobilisation and formation of high grade ore shoots driven by dissolution-reprecipitation replacement and Ni substitution into auriferous arsenopyrite. *Geochim. Et Cosmochim. Acta* **2016**, *178*, 143–159. [CrossRef]

49. Cook, N.J.; Ciobanu, C.L.; George, L.; Zhu, Z.Y.; Wade, B.; Ehrig, K. Trace element analysis of minerals in magmatic-hydrothermal ores by laser ablation inductively-coupled plasma mass spectrometry: Approaches and opportunities. *Minerals* **2016**, *6*, 111. [CrossRef]

50. Wu, Y.F.; Fougerouse, D.; Evans, K.; Reddy, S.M.; Saxey, D.W.; Guagliardo, P.; Li, J.W. Gold, arsenic, and copper zoning in pyrite: A record of fluid chemistry and growth kinetics. *Geology* **2019**, *47*, 641–644. [CrossRef]

51. Cook, N.J.; Chryssoulis, S.L. Concentrations of invisible gold in the common sulfides. *Can. Mineral.* **1990**, *28*, 1–16.
52. Cline, J.S.; Hofstra, A.H.; Muntean, J.L.; Tosdal, R.M.; Hickey, K.A. Carlin-type gold deposits in Nevada: Critical geologic characteristics and viable models. In *One Hundredth Anniversary Volume*; Society of Economic Geologists: Littleton, CO, USA, 2005.
53. Kesler, S.E.; Chryssoulis, S.L.; Simon, G. Gold in porphyry copper deposits: Its abundance and fate. *Ore Geol. Rev.* **2002**, *21*, 103–124. [CrossRef]
54. Bi, S.J.; Li, J.W.; Zhou, M.F.; Li, Z.K. Gold distribution in As-deficient pyrite and telluride mineralogy of the Yangzhaiyu gold deposit, Xiaoqinling district, southern North China craton. *Miner. Depos.* **2011**, *46*, 925–941. [CrossRef]
55. Keith, M.; Smith, D.J.; Doyle, K.; Holwell, D.A.; Jenkin, G.R.; Barry, T.L.; Becker, J.; Rampe, J. Pyrite chemistry: A new window into Au-Te ore-forming processes in alkaline epithermal districts, Cripple Creek, Colorado. *Geochim. Et Cosmochim. Acta* **2020**, *274*, 172–191. [CrossRef]
56. Ohmoto, H. Systematics of sulfur and carbon isotopes in hydrothermal ore deposits. *Econ. Geol.* **1972**, *67*, 551–578. [CrossRef]
57. Hou, M.L.; Jiang, S.Y.; Jiang, Y.H.; Ling, H.F. S-Pb isotope geochemistry and Rb-Sr geochronology of the Penglai gold field in the eastern Shangdong province. *Acta Petrol. Sin.* **2006**, *22*, 2525–2533.
58. Zhang, C.; Liu, Y.; Liu, X.D.; Feng, J.Q.; Huang, T.; Zhang, Q.; Wang, X.D. Characteristics of sulfur isotope geochemistry of the Xincheng gold deposit, Northwest Jiaodong, China. *Acta Petrol. Sin.* **2014**, *30*, 2495–2506.
59. Geng, Y.; Du, L.; Ren, L. Growth and reworking of the early Precambrian continental crust in the North China Craton: Constraints from zircon Hf isotopes. *Gondwana Res.* **2012**, *21*, 517–529. [CrossRef]
60. Xue, J.L.; Pang, Z.S.; Li, S.R.; Chen, H.; Sun, W.Y.; Tao, W.; Yao, L.; Zhang, Y.Q. The genesis of Denggezhuang gold deposit in Jiaodong: Constraints from multigeological chronology and isotope system. *Acta Petrol. Sin.* **2019**, *35*, 1532–1550. [CrossRef]
61. Rowland, J.V.; Sibson, R.H. Structural controls on hydrothermal flow in a segmented rift system, Taupo Volcanic Zone, New Zealand. *Geofluids* **2004**, *4*, 259–283. [CrossRef]
62. Mills, S.E.; Tomkins, A.G.; Weinberg, R.F.; Fan, H.R. Implications of pyrite geochemistry for gold mineralisation and remobilisation in the Jiaodong gold district, northeast China. *Ore Geol. Rev.* **2015**, *71*, 150–168. [CrossRef]
63. Zhu, D.C.; Xu, Q.L.; Lv, D.W.; Yang, S.C.; Yang, Z.Y. The relationship between the Denggezhuang gold deposit's albitite and gold mineralization in the northern section of the Mozhugongka metallogenic belt. *Acta Geol. Sin.* **2018**, *39*, 319–328.
64. Xu, B.; Griffin, W.L.; Xiong, Q.; O'Reilly, S.Y.; Guo, Z.; Zheng, Y.C. Ultrapotassic rocks and xenoliths from South Tibet: Contrasting styles of interaction between lithospheric mantle and asthenosphere during continental collision. *Geology* **2017**, *45*, 51–54. [CrossRef]
65. Xu, B.; Hou, Z.Q.; Griffin, W.L.; Zheng, Y.C.; Wang, T.; Guo, Z.; O'Reilly, S.Y. Cenozoic lithospheric architecture and metallogenesis in Southeastern Tibet. *Earth-Sci. Rev.* **2021**, *214*, 103472. [CrossRef]
66. Tan, J.; Wei, J.; Audétat, A.; Pettke, T. Source of metals in the Guocheng gold deposit, Jiaodong Peninsula, North China Craton: Link to early Cretaceous mafic magmatism originating from Paleoproterozoic metasomatized lithospheric mantle. *Ore Geol. Rev.* **2012**, *48*, 70–87. [CrossRef]
67. Li, L.; Li, S.R.; Santosh, M.; Li, Q.; Gu, Y.; Lü, W.J.; Zhao, G.C. Dyke swarms and their role in the genesis of world-class gold deposits: Insights from the Jiaodong peninsula, China. *J. Asian Earth Sci.* **2016**, *130*, 2–22. [CrossRef]
68. Wang, X.; Wang, Z.; Cheng, H.; Zong, K.; Wang, C.Y.; Ma, L.; Hu, Z. Gold endowment of the metasomatized lithospheric mantle for giant gold deposits: Insights from lamprophyre dykes. *Geochim. Et Cosmochim. Acta* **2022**, *316*, 21–40. [CrossRef]